JOURNAL OF GEOPHYSICAL RESEARCH, VOL. 105, NO. E4, PAGES 9609–9621, APRIL 25, 2000

Identification of a basaltic component on the Martian surface from Thermal Emission Spectrometer data

Philip R. Christensen,[1] Joshua L. Bandfield,[1] Michael D. Smith,[2]
Victoria E. Hamilton,[1] and Roger N. Clark[3]

Abstract. The Mars Global Surveyor Thermal Emission Spectrometer (TES) instrument collected 4.8×10^6 spectra of Mars during the initial aerobraking and science-phasing periods of the mission (September 14, 1997, through April 29, 1998). Two previously developed atmosphere-removal models were applied to data from Cimmeria Terra (25°S, 213°W). The surface spectra derived for these two models agree well, indicating that the surface and atmosphere emission can be separated and that the exact atmosphere-removal model used has little effect on the derived surface composition. The Cimmeria spectra do not match terrestrial high-silica igneous rocks (granite and rhyolite), ultramafic igneous rocks, limestone, or quartz- and clay-rich sandstone and siltstone. A particulate (sand-sized) sample of terrestrial flood basalt does provide an excellent match in both spectral shape and band depth to the Cimmeria spectrum over the entire TES spectral range. No unusual particle size effects are required to account for the observed spectral shape and depth. The implied grain size is consistent with the thermal inertia and albedo of this region, which indicate a sand-sized surface with little dust. The identification of basalt is consistent with previous indications of pyroxene and basalt-like compositions from visible/near-infrared and thermal-infrared spectral measurements. A linear spectral deconvolution model was applied to both surface-only Cimmeria spectra using a library of 60 minerals to determine the composition and abundance of the component minerals. Plagioclase feldspar (45%; 53%) and clinopyroxene (26%; 19%) were positively identified above an estimated detection threshold of 10–15% for these minerals. The TES observations provide the first identification of feldspars on Mars. The best fit to the Mars data includes only clinopyroxene compositions; no orthopyroxene compositions are required to match the Cimmeria spectra. Olivine (12%; 12%) and sheet silicate (15%; 11%) were identified with lower confidence. Carbonates, quartz, and sulfates were not identified in Cimmeria at detection limits of ~5, 5, and 10%, respectively. Their presence elsewhere, however, remains open. The Cimmeria spectra are not well matched by any one SNC meteorite spectrum, indicating that this region is not characterized by a single SNC lithology. The occurrence of unweathered feldspar and pyroxene in Cimmeria, together with the inferred presence of pyroxene and unweathered basalts in other dark regions and at the Viking and Pathfinder landing sites, provides evidence that extensive global chemical weathering of materials currently exposed on the Martian surface has not occurred.

1. Introduction

The Thermal Emission Spectrometer (TES) instrument is a Michelson interferometer/spectrometer that covers the ~6 to 50 μm (1655 to 200 cm^{-1}) wavelength range at moderate (5 and 10 cm^{-1}) spectral resolution. It is designed to study the composition and physical properties of the Martian surface, the composition and abundance of atmospheric aerosols and condensates, the three-dimensional structure of the atmospheric temperature field, and the energy balance and processes in the polar regions [*Christensen et al.*, 1992]. The TES entered Mars orbit on board the Mars Global Surveyor (MGS) spacecraft on September 11, 1997. Over the next 510 days the spacecraft completed a series of 1284 aerobraking and science-phasing orbits in which the orbit was manipulated to achieve the desired mapping orbit with a 350 km altitude and a mean local time of 1400. The data acquired during this period have lower spatial resolution and generally lower surface temperature than those acquired from the 1400 LT nominal mapping orbit. Despite these limitations, these initial data provide new insights into the surface and atmospheric properties of Mars.

In two companion papers we have discussed the techniques and results of the initial efforts to separate the surface and atmospheric components of the measured radiance [*Bandfield et al.*, this issue; *Smith et al.*, this issue]. The first of these papers, by Bandfield et al., provides an estimate of the spectral shape of the dust and water-ice cloud components and demonstrates that TES emissivity spectra can be closely approximated using linear combinations of these spectral shapes. The second paper, by Smith et al., discusses the algorithms for surface-atmosphere separation and derives a suite of surface-only spectra for the classic dark region of Cimmeria Terra. *Smith et al.* [this issue] applied two different methods for sur-

---

[1] Department of Geology, Arizona State University, Tempe.
[2] NASA Goddard Space Flight Center, Greenbelt, Maryland.
[3] U.S. Geological Survey, Denver, Colorado.

Paper number 1999JE001127.
0148-0227/00/1999JE001127$09.00

face-atmosphere separation and tested these techniques using TES data collected under two very different atmospheric temperature and opacity conditions. These atmosphere-removed spectra provide the best determination to date of the thermal infrared spectral properties of the Martian surface.

The purpose of this paper is to provide an analysis of these surface spectra in order to determine the surface mineralogy and petrology within the limits of the current uncertainties in the atmospheric modeling. Cimmeria provides an excellent starting point for the analysis of surface composition because it has a low albedo, and is therefore presumably relatively free of surface dust coatings, and because analysis of previous thermal IR spectral data indicates that dark regions have strong absorption features throughout the TES spectral range [*Christensen*, 1998].

2. Previous Studies

Numerous Earth-based and spacecraft observations have been made of Mars to search for the presence of iron-bearing minerals (see recent reviews by *Soderblom* [1992] and *Bell* [1996]). *Adams* [1974], McCord and coworkers [*McCord et al*., 1982; *Singer et al*., 1979], and *Singer* [1980, 1982] used laboratory and telescopic data to conclude that Ca-rich pyroxenes are likely present and that olivine is not a dominant mineral phase. *Singer and Roush* [1985] identified a broad band centered at 2.1 μm superimposed on the atmospheric CO_2 bands, which they attributed to augite, low-Ca orthopyroxene, or pigeonite. *Erard et al*. [1990], *Mustard et al*. [1990, 1993, 1997], and *Mustard and Sunshine* [1995] used Phobos 2 Infrared Spectrometer for Mars (ISM) data to identify a band between 2.1 and 2.3 μm. *Mustard and Sunshine* [1995] and *Mustard et al*. [1997] analyzed the position and shape of this band and the band from 0.85 to 1.15 μm and argued for the coexistence of low- and high-Ca pyroxene in two dark regions. The occurrence of two pyroxenes is consistent with the composition of the SNC meteorites and suggests a basaltic composition for the regions studied in Eos Chasma and Syrtis Major [*Singer and McSween*, 1993; *Mustard and Sunshine*, 1995; *Mustard et al*., 1997].

Earth-based telescopic thermal-IR observations have suggested a basaltic composition for dark regions in Acidalia Planitia [*Moersch et al*., 1997]. These observations were taken through the Earth's atmosphere, so absolute radiance and emissivity spectra could not be constructed. In addition, these data could not incorporate measurements of the Martian atmospheric temperature and opacity to quantitatively model and remove the Martian atmospheric components. In order to remove the effects of the terrestrial and Martian atmospheres, relative spectra were constructed by ratioing the measured radiance between two different regions [*Moersch et al*., 1997]. As discussed by *Moersch et al*. [1997], this ratio technique cannot uniquely separate an emission minimum in one area from an emission maximum in another. In addition, while ratioing provides a good first-order atmospheric correction, any spectral differences in the atmospheric components or properties between the two areas are mapped into the resultant ratio spectrum. Despite these difficulties, the ratio spectra revealed the presence of a unique component in Acidalia Planitia, whose ratio spectra matched a laboratory thermal emission spectrum of an Antarctic basalt [*Moersch et al*., 1997]. Other dark regions, however, did not show spectral differences from neighboring bright regions [*Moersch et al*., 1997], suggesting that an alternative explanation may exist for the properties observed in the Acidalia Planitia ratio spectrum.

Multispectral thermal-infrared data from the Viking infrared thermal mapper (IRTM) revealed strong absorption features in the 9 and 20 μm IRTM bands [*Christensen*, 1982, 1998]. The depth of these absorptions correlates well with surface markings, with dark regions having the strongest features. The shape of the IRTM four-point spectra is consistent with a basalt-like composition, but these data lacked sufficient spectral resolution to accurately model the atmosphere or uniquely identify the surface composition [*Christensen*, 1998].

Previous analyses of the Martian surface and SNC meteorites have provided indirect evidence that components with basaltic to andesitic compositions are present on Mars. In situ spectral observations have been made of Mars at three landing sites (Viking 1 and 2 and Pathfinder) that also provide indirect evidence for mafic compositions. In particular, Viking multispectral data of dark rocks are consistent with unoxidized basaltic andesite, although this match is not unique [*Adams et al*., 1986; *Guinness et al*., 1987, 1997]. In situ X-ray flourescence (XRF) measurements of soils at the Viking landing sites indicated low silica abundances (42–44% SiO_2) that are broadly consistent with basaltic compositions [*Clark et al*., 1982], although attempts to match the compositional pattern of the soils to terrestrial, lunar, and meteorite rock compositions have not provided satisfactory matches [*Banin et al*., 1992]. Several shergottites, widely accepted as samples ejected from the Martian surface, are basaltic in composition. Shergotty, Zagami, and EET79001 consist primarily of pyroxene (augite and pigeonite) and plagioclase feldspar [*Smith and Hervig*, 1979; *Stolper and McSween*, 1979; *Stöffler et al*., 1986]. Relative to terrestrial basaltic compositions, these rocks have low Al_2O_3 contents and high bulk Fe/(Fe + Mg) ratios [*McSween*, 1994]. X-ray mode measurements by the Mars Pathfinder alpha proton X-ray spectrometer (APXS) of five rocks at the landing site provide silica contents ranging from $\sim$52 to 61% SiO_2 [*Reider*, 1997], which are considerably more felsic than the Viking soils. Analyses of the Pathfinder data by *McSween et al*. [1999] suggest that the best classifications for the Pathfinder rocks range from basaltic andesite to andesite, with an andesitic sulfur-free rock composition.

Taken together, the previous spectral observations have made a strong case for the presence of pyroxenes in dark regions on Mars and have provided indirect evidence for basalts or andesites on the surface.

3. TES Data

3.1. Instrument Overview

The TES instrument consists of three subsections: (1) a Michelson interferometric spectrometer; (2) a bolometric thermal radiance (4.5 to $\sim$100 μm) channel; and (3) a solar reflectance (0.3 to 2.7 μm) channel. Data are collected from six detectors, each with an $\sim$8.5 mrad instantaneous field of view (IFOV), in each boresighted instrument subsection during one observation period (2 s). These IFOVs provide a contiguous strip three elements wide with a spatial resolution designed to be 3 km in the final MGS mapping orbit altitude of 350 km. Observations are time ordered using orbit number (Pn), which corresponds to one revolution of the spacecraft around Mars, and an incremental counter (ICK) which begins at one on each orbit. The data discussed in this paper are among the 4.8×10^6 spectra collected during the aerobraking phase of the MGS mission on orbits P3 through P268 (September 14, 1997, through April 29, 1998), corresponding to the Aerobraking Phase 1 (AB1) and Science Phasing Orbits 1 (SPO1) of the MGS mission. These orbits occurred during the southern spring and summer seasons (aerocentric longitude (L_s) 182°–319°). In this paper the radiance data have been converted to emissivity by assuming unit emissivity at the point of maximum brightness temperature within the TES spectral range.

3.2. Radiance Precision and Accuracy

The 1-sigma radiance precision of an individual spectral sample in a single TES spectrum has been determined using both prelaunch and in-flight observations to be $\sim 2.5 \times 10^{-8}$ W cm^{-2} str^{-1}/cm^{-1} from ~300 to 1400 cm^{-1}, increasing to $\sim 6 \times 10^{-8}$ W cm^{-2} str^{-1}/cm^{-1} at 250 cm^{-1} and to $\sim 4 \times 10^{-8}$ W cm^{-2} str^{-1}/cm^{-1} at 1650 cm^{-1} [*Christensen*, 1999]. Systematic errors in radiance can occur because of the calibration process, in which periodic views of space and an internal reference surface are used to determine the instrument response function and the instrument radiance [*Christensen and Harrison*, 1993]. The instrument noise in these measurements maps into each of the calibrated planet spectra in a complex way that is a function of the instrument temperature and the temperature difference between the scene and the instrument. This noise is reduced by (1) acquiring and averaging three consecutive observations of both space and the reference surface and (2) interpolating the instrument response function for successive calibration observations (typically 10–60 min apart during SPO1).

The instrument temperature during the SPO1 orbits varied from 283 to 288 K, and the surface temperature of the spectra presented here ranged from 275 to 285 K. For this combination of temperatures the resulting systematic calibration error is $\sim 1 \times 10^{-8}$ W cm^{-2} str^{-1}/cm^{-1} between 300 and 1400 cm^{-1}. The spectra presented in this paper are averages of at least one spectrum from each of the six individual detectors. With this averaging the total error due to the combined random and systematic errors is reduced to $\sim 1.2 \times 10^{-8}$ W cm^{-2} str^{-1}/cm^{-1} between 300 and 1400 cm^{-1}.

These radiance errors can be converted to emissivity errors which vary with wavenumber due to the variation in blackbody radiance with temperature and wavenumber. For a surface temperature of 280 K the total error from random and systematic sources is <0.0013 from 300 to 1100 cm^{-1}, increasing to 0.0035 at 1400 cm^{-1} for averages of six spectra.

The absolute accuracy of the TES spectra was determined prelaunch to be $\sim 4 \times 10^{-8}$ W cm^{-2} str^{-1}/cm^{-1} from ~300 to 1400 cm^{-1} [*Christensen*, 1999]. For a surface temperature of 280 K, this error corresponds to an absolute temperature error of 0.5 K. This temperature error is mapped into a smoothly varying offset in the emissivity spectrum that varies from 0.001 at 400 cm^{-1} to a maximum of 0.004 at 920 cm^{-1} to essentially 0 at 1300 cm^{-1}. This subtle curvature has a negligible effect on the derived surface composition. A second systematic accuracy error is present owing to slight variations in the instrument radiance between views of space, the reference surface, and the planet. The TES secondary mirror rotates with the pointing mirror [*Christensen et al.*, 1992], and, as a result of a slight misalignment of the optical axis with the rotational axis of this mirror, the fraction of the instrument viewed in each orientation varies slightly. The consequence is a background radiance error of $\sim 1.0 \times 10^{-8}$ W cm^{-2} str^{-1}/cm^{-1} between ~300 and 1400 cm^{-1}.

3.3. Surface-Atmospheric Separation

In the companion paper by *Smith et al.* [this issue], two models were developed for separating the surface and atmospheric components of TES spectra. These models are referred to as the radiative transfer and deconvolution algorithms. Both methods use atmospheric dust and water-ice cloud spectral properties that were determined independently. These properties have been shown to be constant in space and time over a wide range of atmospheric conditions [*Bandfield et al.*, this issue], which greatly simplifies the atmospheric modeling.

The atmospheric dust spectrum was isolated using factor analysis and target transformation techniques on TES spectra from a wide range of surfaces and atmospheric dust and loading [*Bandfield et al.*, this issue]. This dust spectrum is interpreted to contain little, if any, surface spectral character on the basis of (1) the close similarity between the derived dust spectrum and spectra acquired with high dust opacity and/or with high emission angles in which the atmospheric dust dominates the spectrum; (2) the good agreement between the derived atmospheric dust spectrum and TES limb spectra that view only the atmosphere; (3) the consistent surface spectra derived using this dust spectrum for atmospheric dust opacities that varied by a factor of 5–10; and (4) the consistent atmospheric dust spectra in pairs of day/night observations in which the dust is alternately viewed in transmission and emission. Diurnal measurements from the Viking IRTM instrument have also been used to separate the spectral properties of surface and atmospheric dust [*Christensen*, 1982] and have shown that the emissivity of bright regions is high (>0.99) and spectrally flat in the wavelength region studied here. The uncorrected TES spectra of bright regions closely match the derived atmospheric dust spectrum, which is consistent with the spectral character of these regions. Finally, while the surface materials in bright regions are likely to be accumulations of airborne dust [*Christensen*, 1985], the spectra of these materials viewed in emission on the surface will differ significantly from the spectrum of the same materials viewed in emission/transmission when suspended in the atmosphere. We conclude therefore that it is unlikely that any significant surface component is being removed with the atmospheric correction [*Smith et al.*, this issue].

The radiative transfer algorithm uses radiative transfer and successive least squares fitting to model the spectral properties of atmospheric dust, atmospheric water ice, and surface emissivity in each TES spectrum [*Smith et al.*, this issue]. The deconvolution algorithm assumes that the TES spectra are linear combinations of atmosphere and surface spectral shapes, as demonstrated by *Bandfield et al.* [this issue]. The atmospheric dust and water-ice spectral shapes are combined with a suite of laboratory mineral spectra to make an endmember library. This library is fit to the TES emissivity spectrum using a linear least squares best fit deconvolution algorithm [e.g., *Adams et al.*, 1986; *Ramsey and Christensen*, 1998] to determine the abundances of all components. The atmospheric components are then removed in accordance with their derived abundances to give a surface-only spectrum [*Smith et al.*, this issue]. The spectral range was limited to 400–1280 cm^{-1} in these analyses owing to limitations in the current spectral library and to the effect of variable atmospheric water vapor, which is not currently modeled.

An example of the best fit of the radiative transfer algorithm for the classic bright region of Isidis Planitia (9°N, 276°W) is shown in Figure 1. This fit was achieved using only atmospheric

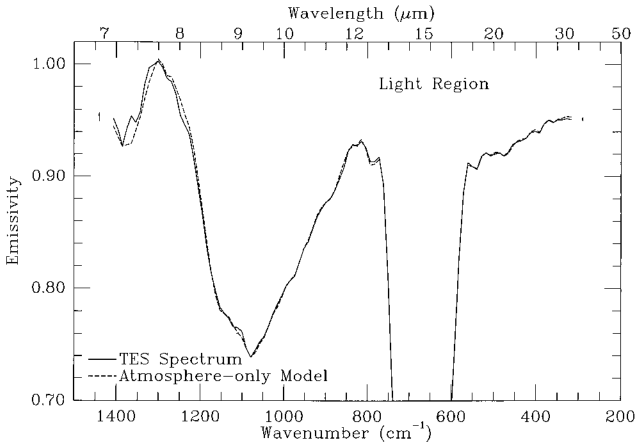

Figure 1. Modeling of bright region spectra. The solid line is a TES spectrum from the average of the six detectors collected on orbit P61, ICK 785, from the Isidis Planitia region at 9.2°N, 276°W. These data are compared to a radiative transfer model (dotted line) that uses only atmospheric components: CO_2, atmospheric dust, and water ice. For this region the atmosphere-only model can reproduce the data to within the noise level.

dust, clouds, and CO_2. As seen in Figure 1, the "atmosphere-only" model fits the data to within the instrument noise level (see section 3.2), indicating that the atmosphere-only model does an excellent job of accounting for (and removing) the observed spectral signature for regions where the surface materials have low-contrast spectra from 400 to 1280 cm^{-1}.

Figure 2 shows the results of modeling spectra from the dark region in Cimmeria Terra, centered on 25°S, 213°W, again using the radiative transfer algorithm. The atmosphere-only model provides a poor fit to the TES spectrum (Figure 2a), which indicates that the surface is adding a significant spectral contribution. Figure 2b shows the fit achieved for the Cimmeria region using a combined surface and atmosphere model. In this case the fit is significantly improved, and the model reproduces the TES spectrum to within the level of the instrument noise. Similar modeling of a hematite-rich region near 0°N, 0°W [*Christensen et al.*, this issue (b)] also reproduced the spectra from that area using a combination of atmospheric and mineralogic components [*Christensen et al.*, this issue (b)].

3.4. Atmosphere-Removed Surface Spectra

Smith et al. [this issue] derived atmosphere-removed, surface-only spectra for the dark region in Cimmeria Terra at 24.8°S, 213.3°W, using both the radiative transfer and deconvolution algorithms. Data were collected of this region with an infrared atmospheric dust opacity τ_{IR}, measured by TES at 9 μm, of 0.11 (P219) and 0.33 (P56) and with different water-ice abundance and atmospheric temperatures. Both atmosphere-removal models were applied to the two different atmospheric conditions, yielding four independent derivations of the surface-only spectrum [*Smith et al.*, this issue].

An estimate of the errors in the surface spectra due to the combined instrumental and atmospheric modeling effects can be obtained by comparing the four surface spectra derived from the two atmospheric-removal models by *Smith et al.* [this issue]. These surface spectra are in excellent agreement, despite being derived from two models with widely different approaches and mathematical derivations and under very different atmospheric dust and water-ice loadings [*Smith et al.*, this issue]. Figure 3a gives the mean and ±1-sigma variation in the surface spectra derived for these four cases. All of the random and systematic instrumental uncertainties in the original spectra, as well as the uncertainties produced by the different atmospheric-removal models, are included in these spectra. Thus the 1-sigma variation in these models provides a good assessment of the total uncertainty in the derived surface spectra. Error bars corresponding to the ±1-sigma values in Figure 3a are included on all subsequent surface-only spectra.

The surface spectra derived for the low atmospheric dust case using both the radiative transfer and deconvolution models are reproduced from *Smith et al.* [this issue] in Figure 3b and are the basis for the mineralogic analysis presented in the following sections.

4. Results

4.1. Rock Type Classification of TES Spectra

Figure 4 shows a comparison of the surface spectra (deconvolution algorithm) from Cimmeria with a suite of represen-

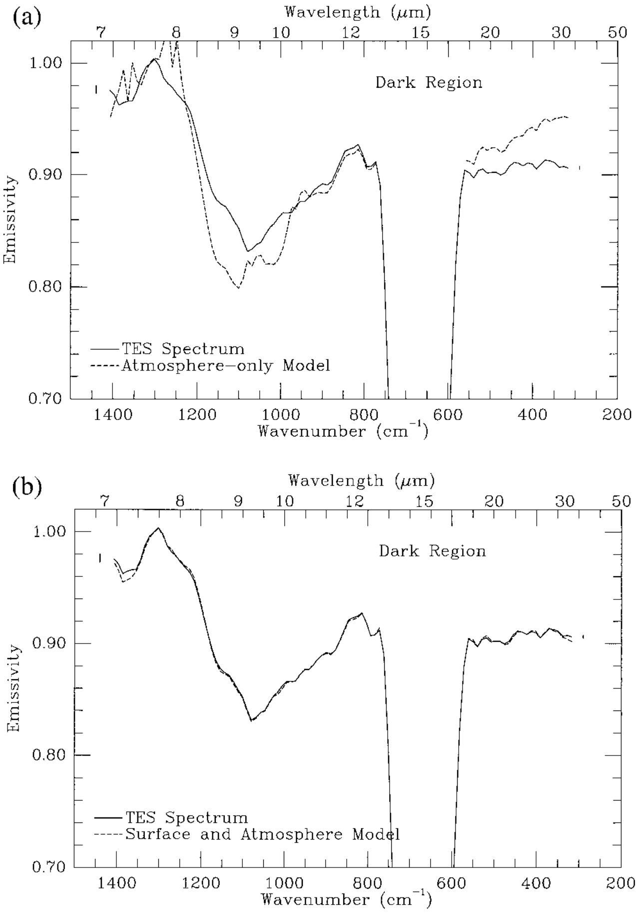

Figure 2. Modeling of dark region spectra. (a) A TES spectrum from the average of the six detectors collected from Cimmeria Terra (24.8°S, 213.2°W) on orbit P219, ICK 1675, (solid line) has been modeled using the atmosphere-only radiative transfer model (dashed line). In this case the atmosphere-only model cannot reproduce the overall spectrum, indicating that surface spectral features are present. (b) A model incorporating both atmospheric and surface components (dashed line) provides an excellent fit to the TES spectrum.

tative sedimentary and igneous rocks. Figure 4a shows the TES spectrum compared to extrusive and intrusive igneous rocks of high-silica (rhyolite and granite) and low-silica content (basalt and gabbro), as well as quartz-rich sandstone, siltstone, and carbonate limestones. These different rock types have significantly different spectra, with variations within each class that are smaller than the variations between classes [*Lyon and Burns*, 1963; *Hovis et al.*, 1966; *Hunt and Salisbury*, 1975, 1974; *Salisbury et al.*, 1988; *Feely and Christensen*, 1999]. These differences allow the different major rock types to be distinguished even without the use of complex spectral analysis algorithms. For example, the sedimentary rocks are made up largely of quartz (sandstones and siltstones) or carbonate (limestone) minerals, with low abundances of feldspar and mafic minerals. As a result, their spectra are distinctly different from the igneous rocks, which are dominated by feldspar, pyroxene, and olivine. Within the igneous suite, there are major differences in the relative abundance of quartz, feldspar, pyroxene, and olivine, which again results in distinct differences in the overall rock spectra.

A qualitative comparison of the spectra in Figure 4a shows that several common terrestrial rock compositions, such as sandstones, siltstones, limestones, and granite, can be immediately excluded as potential matches to the Cimmeria spectra. Figure 4b shows the Cimmeria spectrum compared to a suite of igneous extrusive rocks with compositions varying from rhyolite to weathered komatiite. Several members of this suite can be eliminated by their poor match to the TES spectrum, including rhyolite, dacite, and weathered komatiite. The basalt sample, however, provides an excellent match to the Cimmeria spectrum. This flood basalt is a particulate sample acquired from the Deccan Plateau [*Hamilton and Christensen*, this issue]. Figure 5 shows the direct comparison of the flood basalt and Cimmeria spectra; the agreement of both the shape and depth of spectral features between the two is remarkable. As discussed in the following sections, this qualitative determination of rock type agrees well with the quantitative mineral abundances derived from deconvolution modeling.

4.2. Quantitative Mineralogic Identification: Laboratory Example

The analysis of TES spectra can be extended well beyond the simple recognition of rock type shown in Figures 4 and 5. Deconvolution of thermal infrared spectra has been demonstrated to provide an accurate estimate of mineral abundance both for mixtures of granular materials of a wide range of particle sizes [e.g., *Thomson and Salisbury*, 1993; *Ramsey and Christensen*, 1998] and for rocks of varying composition and grain size [*Feely and Christensen*, 1999; *Hamilton and Christensen*, this issue]. The absolute errors in mineral determinations are estimated to be ±5–15% in both the petrographic and laboratory spectroscopic [*Ramsey and Christensen*, 1998; *Feely*, 1997; *Hamilton and Christensen*, this issue] methods.

As an example of the deconvolution method for basaltic rocks, a suite of 59 pure minerals from the Arizona State University (ASU) mineral library [*Christensen et al.*, this issue (a)] was used to deconvolve the Deccan flood basalt sample. This mineral suite contains members of the major mineral groups, including 11 plagioclase and alkali feldspars, 15 orthopyroxenes and clinopyroxenes, olivines, quartz, sheet silicates, amphiboles, carbonates, oxides, and sulfates (Table 1). Note that our library did not include pigeonite owing to difficulties in obtaining a pure sample. Rock and particulate samples often have lower spectral contrast than the library minerals owing to the large size (710–1000 μm) of the particles used for the library. A blackbody component was included in the spectral library to allow for reduced spectral contrasts in the unknown spectra [*Hamilton et al.*, 1997; *Ruff*, 1998]. Its purpose is to account for the fact that the band depths in pure, coarse-grained minerals can be deeper, in a constant ratio throughout the entire spectrum, than those in fine-grained rocks and granular material. Without a blackbody component the deconvolution algorithm erroneously selects minerals with flat spectra in an attempt to model the fact that the depths of all bands are consistently decreased [*Hamilton et al.*, 1997; *Ruff*, 1998].

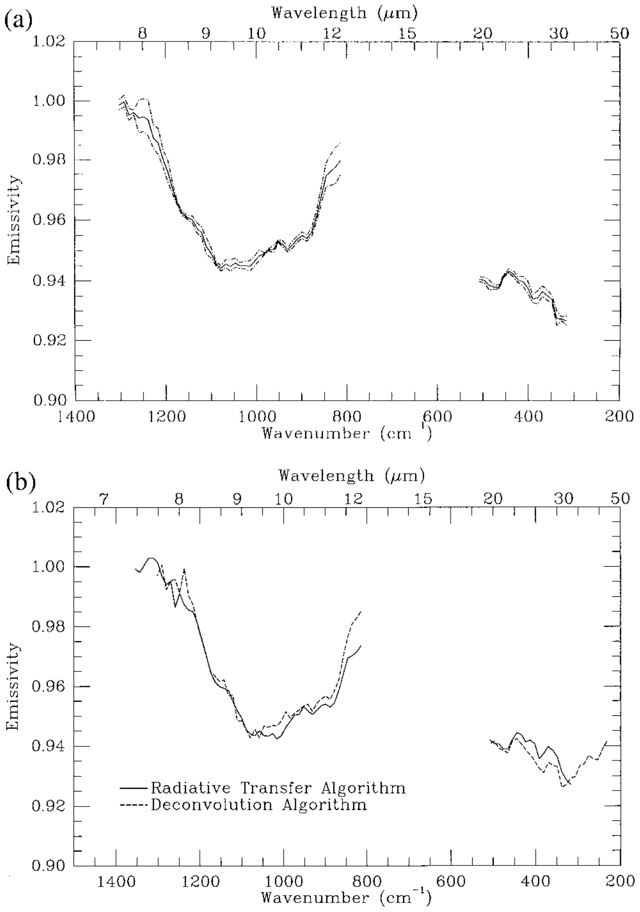

Figure 3. Atmosphere-removed spectra of Cimmeria Terra. (a) Mean and ±1-sigma variation in the four atmosphere-removed spectra derived by *Smith et al.* [this issue] using the radiative transfer and deconvolution algorithms for two different atmospheric dust opacities. (b) The low-atmospheric dust (τ = 0.1) case for the radiative transfer and deconvolution algorithms reproduced from *Smith et al.* [this issue].

The spectra of both the Deccan sample and the mineral library were convolved to TES 10 cm^{-1} sampling and the CO_2 band was excluded in order to provide a realistic comparison to TES data modeling. The spectral deconvolution of the Deccan flood basalt rock sample is shown in Figure 6. A comparison of the mineral abundances derived from petrographic analysis ("known") and the linear deconvolution model is given in Table 2. The deconvolution model identified the two dominant minerals, plagioclase feldspar and high-Ca pyroxene, that are present above a 10% detection limit. The feldspar abundance

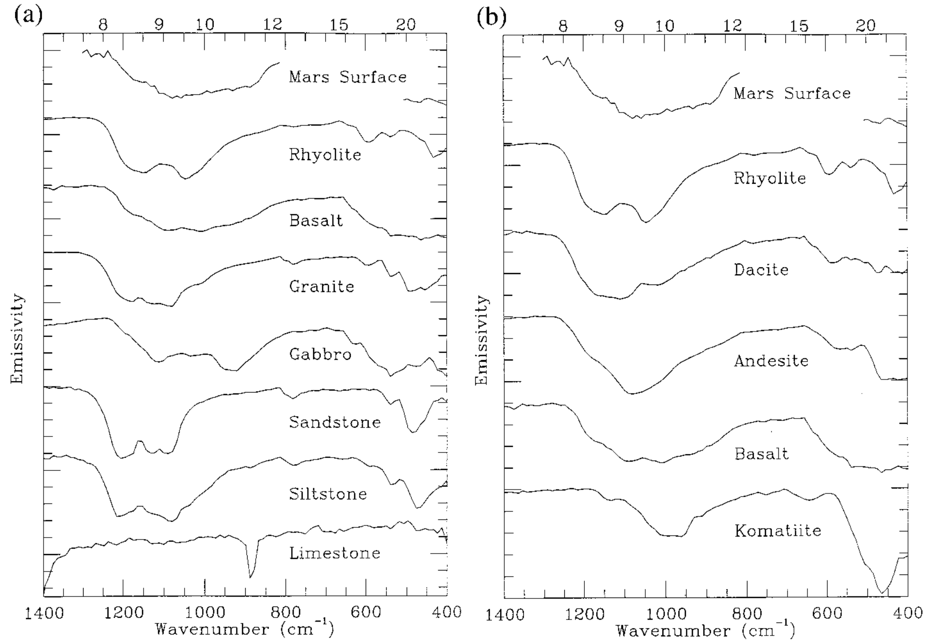

Figure 4. Comparison of Cimmeria Terra surface-only spectrum with a suite of rocks of different composition. (a) General rock suite including high- and low-silica rocks of intrusive and extrusive origin and sedimentary rocks of varying quartz, clay, and carbonate content. It is apparent from this comparison that high-silica (e.g., sandstone, siltstone, granite, and rhyolite) and carbonate compositions can be excluded in the Cimmeria region. (b) Comparison of Cimmeria spectrum with a suite of extrusive igneous rocks. The best fit to Cimmeria Terra is a basaltic composition.

was determined to well within the accuracy of either analysis method; the pyroxene abundance differs by 11% but is within the combined uncertainties of the petrographic (±5–10% [*Feely*, 1997]) and spectroscopic [*Ramsey and Christensen*, 1998; *Feely*, 1997; *Hamilton and Christensen*, this issue] techniques. A portion of this difference is likely due to the fact that the spectroscopic measurement was taken of a broken surface, which tends to emphasize intergrain weathering products such as Fe-smectite. The blackbody abundance was 42%, which is consistent with that typically found for fine-grained rock samples [*Ruff*, 1998; *Feely and Christensen*, 1999; *Hamilton and Christensen*, this issue].

Comparison of the rock and best fit model spectra with the spectra of the end-member minerals illustrates how the fine-scale structure of the individual mineral spectra combines linearly to produce a complex rock spectrum with reduced modulation (Figure 6). As a result, most rock and mixed-particulate samples are difficult to analyze using simple comparisons of individual spectral band shapes to those of individual minerals. However, the component minerals can be identified by a simultaneous, least squares solution for all minerals present in the sample [*Adams et al.*, 1986; *Gillespie et al.*, 1990; *Ramsey and Christensen*, 1998; *Feely and Christensen*, 1999; *Hamilton and Christensen*, this issue]. Thus, while the spectra of basalts and andesites appear to have broad spectral features (Figure 4), these spectra are uniquely matched only by their constituent minerals, and the abundance of the major mineral components can be determined to within standard petrographic accuracies.

4.3. Quantitative Mineralogic Identification: Cimmeria

The deconvolution model was applied to the two Cimmeria surface-only spectra derived from the atmospheric-removal algorithms using the suite of minerals listed in Table 1. The surface-only spectra and best fit models are compared in Figure 7, and the derived mineral abundances are given in Tables 3a and 3b. Blackbody abundances of 54 and 47% were required to fit the radiative transfer and deconvolution models, respectively. As with the Deccan flood basalt sample, these values are consistent with the values typically found for particulate materials [*Ramsey and Christensen*, 1998]. Rounding errors of ±1 result in total abundances that differ from 100%.

The deconvolution analysis identified a total of 14 different

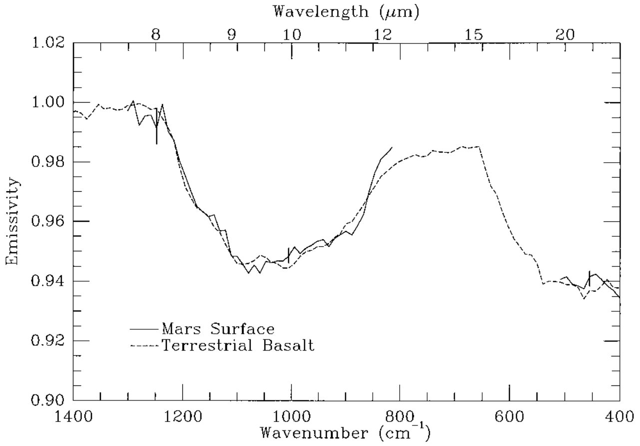

Figure 5. Comparison of a particulate Deccan flood basalt sample and Mars Cimmeria Terra spectra. No scaling, contrast enhancement, or continuum removal has been applied to either spectrum. The shape and spectral contrast of the TES and Deccan basalt match well.

Table 1. TES Spectral Deconvolution Mineral Suite

Mineral	ASU Sample
Plutonic Quartz	···
Vein Quartz	···
Microcline	BUR-3460A
Perthite	WAR-5802
Orthoclase	AK-01
Albite	WAR-0612
Albite	WAR-0235
Oligoclase	WAR-0234
Andesine	WAR-0024
Labradorite	BUR-3080A
Labradorite	WAR-4524
Bytownite	WAR-1384
Anorthite	BUR-340
Actinolite	HS-315.4B
Jade (Nephrite)	WAR-0979
Anthophyllite	BUR-4760
Magnesio-hornblende	WAR-0354
Magnesio-riebeckite	HS-326.4B
Hornblende	BUR-2660
Amphibole	ASU-03
Magnesio-hornblende	WAR-0390
Amphibole	NMNH-R7208
Goethite	NMNH152500:
Biotite edges	BUR-840
Biotite face	BUR-840
Muscovite face	MLC
Phlogopite face	MLC
Chlorite	WAR-1924
Serpentine	NMNH-47108
Enstatite	HS-9.4B
Enstatite	DSM-ENS01
Enstatite	NMNH-34669
Bronzite	BUR-1920
Bronzite	NMNH-119793
Bronzite	NMNH-C2368
Augite	WAR-6474
Augite	HS-119.4B
Augite	NMNH-119197
Augite	NMNH-9780
Magnesian-hedenbergite	DSM-HED01
Magnesian-hedenbergite	NMNH-R11524
Diopside	BUR-1820
Diopside	WAR-5870
Diopside	NMNH-R17421
Johannsenite	BUR-2883
Jadeite	WAR-9909
Spodumene	WAR-7684
Epidote	BUR-1940
Forsterite	BUR-3720A
Fayalite	WAR-FAY01
Hematite	···
Anhydrite	ML-S9
Gypsum	ML-S8
Calcite	ML-C9
Dolomite	C17
Kaolinite	KGa-1b
Nontronite	WAR-5108
Fe-smectite	SWa-1
Illite	IMt-2
Blackbody	

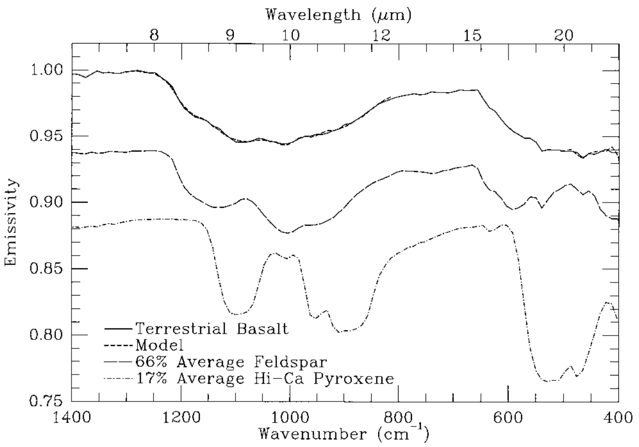

Figure 6. Spectral deconvolution of a laboratory Deccan basalt sample. Measured (solid line) and modeled (short-dashed line) spectra are shown, together with the spectra of the major component minerals. This sample is composed primarily of feldspar and pyroxene (Table 2), whose abundances are accurately determined by spectral deconvolution. While the component minerals have distinct spectral features from 8 to 12 μm, the resultant rock spectrum is more complex and the individual bands are less obvious. The simultaneous, least squares deconvolution, however, provides an excellent fit to the rock spectrum and gives an accurate determination of the mineral composition and abundance.

minerals from the suite listed in Table 1 using the two surface spectra. These included four feldspars of slightly different composition and two clinopyroxenes. Typically, several different feldspars and pyroxenes are identified by the deconvolution algorithm in order to give the best fit (lowest RMS) match to an unknown spectrum. However, the precision to which the composition and abundance of these individual mineral species are identified exceeds the true accuracy of the deconvolution analysis (see section 4.4). We have chosen therefore to group some minerals into broader mineral classes.

The primary mineral identified in both surface-only spectra was feldspar, with abundances of 45 and 53%. A combination of plagioclase (>~85%) with minor (<15%) alkali feldspar provided the best match in both surface spectra. Given the preponderance of plagioclase in the total derived feldspar abundance, we interpret the results to indicate that plagioclase is the feldspar present on Mars. However, a more detailed assessment of the plagioclase composition is unwarranted at this time.

The second most abundant mineral is clinopyroxene (19%; 26%), with a combination of augite and minor diopside providing the best fit in the deconvolution model. Olivine (12%) and sheet silicates (11%; 15%) were also selected in the best fit match to the TES spectra.

4.4. Abundance Limit Uncertainty Estimate

The formal error in mineral abundance derived using thermal IR spectroscopic measurements under optimum laboratory conditions has been estimated to be ±5–15% [*Ramsey and Christensen*, 1998; *Feely and Christensen*, 1999; *Hamilton and Christensen*, this issue]. This uncertainty is different for each

Table 2. Modal Results for Deccan Basalt Sample

Minerals	Known Percentage*	Model Percentage
Plagioclase Feldspar	65	66
Ca Pyroxene	28	17
Opaques	4	0
Fe-Smectite	0	7
Other	3	10
Total	97	100

*From *Hamilton and Christensen* [this issue].

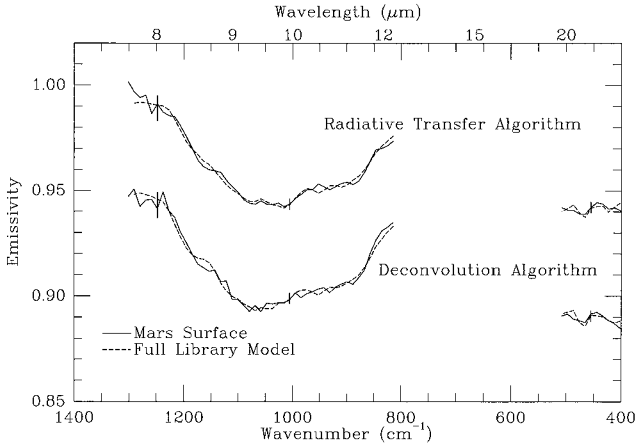

Figure 7. Spectral deconvolution of the TES Cimmeria Terra spectra using the full mineral library (Table 1). The best fit model results for the surface spectra derived from both atmospheric-removal algorithms are shown. The abundances of the best fit minerals are given in Table 3a.

mineral depending on the strength, width, and position of the spectral features, as well as the spectral properties of the other minerals present. This uncertainty must increase at Mars owing to the uncertainties in the current atmospheric-removal models, the restriction in wavelength range due to atmospheric gases, and the lower spectral resolution of the TES compared to laboratory instruments. The single example shown in Figure 6 of a laboratory sample under simulated TES observing conditions provides insight into the absolute accuracy of TES-derived mineral abundances and suggests that accuracies of ~10% can be achieved.

One estimate of the uncertainties in the model fits is provided by the RMS difference between the best fit model and the data (Table 3a). The RMS emissivity error in the fits shown in Figure 7 and listed by mineral abundance in Table 3a is 0.0020 for the radiative transfer model and 0.0023 for the deconvolution model. The RMS error provides a formal measure of the goodness of fit but does not necessarily provide the best assessment of the quality of a model fit. While mathematically robust, this parameter does not account for offsets in spectral bands due to small differences in end-member composition or for slopes or other low-frequency differences between the observed and modeled spectra. As a result, two model fits might have similar RMS errors, but one can be identified by visible inspection to provide a better match to the spectral structure, phase, and slope. Thus, for example, a model fit in which each band is present but is offset slightly in frequency or band depth from the unknown spectrum can have a higher RMS error than a fit in which there is no correlation between any absorption features.

Table 3a. Deconvolution Analysis: Full Library

Mineral	Radiative Transfer Model	Deconvolution Model
Quartz	2	3
Plagioclase Feldspar	53	45
Clinopyroxene	19	26
Olivine	12	12
Sheet Silicate	11	15
Gypsum	2	0
Total	99	101

Table 3b. Deconvolution Analysis: Feldspar/High-Ca Pyroxene Library Subset

Mineral	Radiative Transfer Model	Deconvolution Model
Plagioclase Feldspar	65	56
Clinopyroxene	35	44
Total	100	100

The most significant estimate of the mineral abundance uncertainty comes from the comparison of the mineral abundances derived for the two different atmosphere-removed surface spectra. These spectra are representative of the ±1-sigma errors shown in Figure 3a and therefore provide a quantitative estimate of the uncertainty due to the entire analysis process, from instrument noise through the atmospheric removal. The resulting variations in the derived mineral abundances (Table 3a) provide a realistic estimate of the accuracy and precision (e.g., the "science to noise ratio") to which different minerals can be determined.

Variations of 7–8% are seen in the feldspar and pyroxene abundances. Olivine and sheet silicates were modeled near the detection limit in both cases and agree to within 0 and 4%, respectively. Minor gypsum was "detected" in the radiative transfer model, but its abundance is below our estimate of a reliable detection limit for this mineral. Overall, the differences between mineral abundances derived from the two atmospheric-removal models are small, and the exact nature of the atmospheric removal model used has little effect on the derived surface composition.

A third measure of the sensitivity of the derived mineral abundances to spectral variations and noise can be illustrated using models in which the abundances of the different minerals are varied. These variations are illustrated in Figure 8 for a set of models in which the abundance of the primary components, pyroxene and plagioclase feldspar, are varied in offsetting increments while keeping the other components fixed at their best fit values. Variations of 10% abundance show significant differences from the TES data in the region from 400 to 500

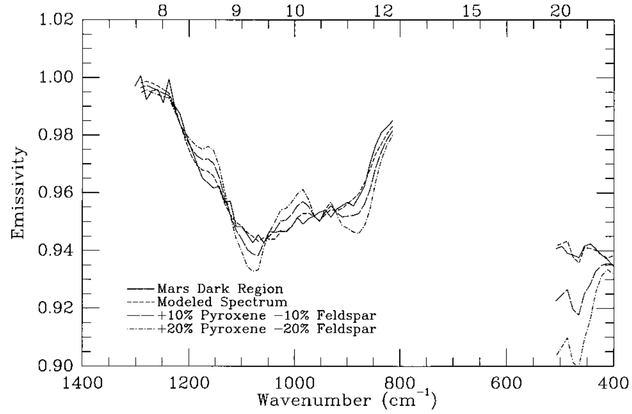

Figure 8. Comparison of TES Cimmeria spectrum with models in which the abundance of pyroxene and feldspar are varied in offsetting increments while keeping the other components fixed at their best-fit values.

cm^{-1}. In the 800–1300 cm^{-1} region the differences are smaller but are larger than the instrument noise and the uncertainty produced by the different atmospheric corrections (Figure 3). Variations of 20% in the pyroxene and feldspar abundance differ significantly from the TES spectrum, which indicates that 10–20% is an upper limit on the ability to accurately model these components.

As a final test of the net effect of the minor components on the quality of the overall fit, the deconvolution algorithm was run using a reduced end-member suite consisting of only the feldspar and high-Ca pyroxene members of the spectral library. The resultant best fit spectra are given in Figure 9 for both atmospheric separation models, and the derived mineral abundances are given in Table 3b. The quality of the fit is only slightly degraded in these reduced-end-member models, with RMS emissivity errors of 0.0023 and 0.0032 versus 0.0020 and 0.0023 for the full mineral suite. Visual inspection of the reduced-model fits shows that they reproduce all of the major spectral features in the data, although the overall quality of the fit is lower. Limiting the model to only the feldspar and pyroxene end-members obviously forces the abundance of these components to increase. Comparing the full- and reduced-library results shows that the feldspar abundance increases by 11–12% and the pyroxene abundance increases by 16–18% in the reduced library model (Tables 3a and 3b). These values provide an additional estimate of the absolute accuracy to which these minerals are currently being modeled. The feldspar composition was again dominated (>85%) by plagioclase minerals, and the best fit pyroxenes included augite and minor diopside.

In summary, on the basis of these results we estimate that the mineral abundance accuracy and detection threshold are 10–15% for the actual TES instrument noise and the uncertainties in the current atmospheric-removal models. This value is in agreement with other estimates of the uncertainties in deconvolution methods [*Ramsey*, 1996; *Feely*, 1997; *Feely and Christensen*, 1999; *Hamilton and Christensen*, this issue], after accounting for the fact that the TES was viewing a relatively cold surface through an atmosphere with significant dust, water-ice, and CO_2 opacity.

5. Discussion

5.1. Basalt Component

Surface spectra of the Cimmeria region derived using two entirely different models to remove the atmospheric components of dust, water ice, and CO_2 under two different atmospheric dust loads give surface spectra that are self-consistent to within the level of uncertainty in these models and the instrument noise. The qualitative match of these TES surface spectra to the spectrum of basalt (Figures 4 and 5), without any further modeling, provides excellent evidence for a basaltic material exposed on the surface of Mars.

Detailed modeling of the surface spectra shows that a mixture of feldspar, dominated by plagioclase, clinopyroxene (augite and diopside), ±olivine, and ±sheet silicates, provides the best fit to the TES spectra. The two different atmospheric-removal models identified the same minerals, providing strong evidence that the general character of this mineralogic identification of surface materials is independent of the atmospheric-removal modeling. A surface of only plagioclase feldspar and clinopyroxene can account for the overall spectral properties observed given the instrument noise and uncertainties in the current atmospheric modeling. Therefore the olivine and sheet silicate components, while possibly present, cannot be reliably identified at this time.

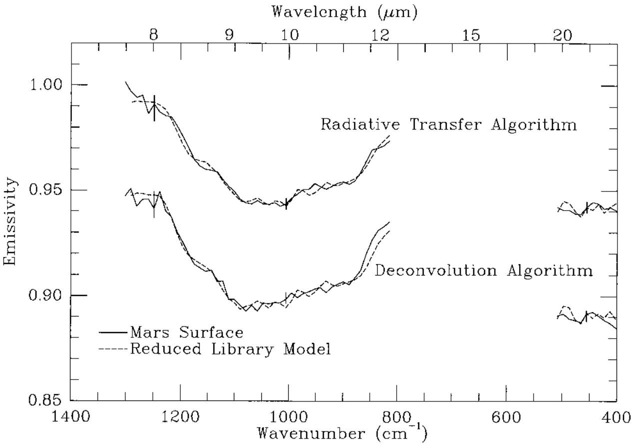

Figure 9. Spectral deconvolution of the TES Cimmeria Terra spectra using a subset of the mineral library having only high-Ca pyroxene and feldspar minerals.

It is important to note that the spectral contrast of the Martian surface spectra closely matches the contrast observed in laboratory samples of basaltic sand. No scaling, contrast enhancement, or continuum removal was applied to either spectrum shown in Figure 5. Thus the spectra observed by the TES instrument are consistent with what is expected for particulate basaltic materials on the surface, and no unusual particle-size or other environmental effects are observed in these data. This match in band depth, as well as shape, provides additional evidence that all of the major surface components have been identified.

Despite the evidence presented here, the possibility remains that the spectral match to plagioclase, pyroxene, olivine, and sheet silicates is fortuitous and that the Mars surface is made up of a different suite of minerals whose collective spectral properties mimic those of basalt. However, terrestrial experience with thermal infrared spectra does not support such fortuitous matches for rocks [*Lyon and Burns*, 1963; *Hovis et al.*, 1966; *Hunt and Salisbury*, 1974, 1975; *Salisbury et al.*, 1988; *Feely and Christensen*, 1999], particulate samples [*Thomson and Salisbury*, 1993; *Ramsey and Christensen*, 1998], or remote-sensing observations [*Gillespie et al.*, 1984; *Hook et al.*, 1994; *Ramsey et al.*, 1999]. No other combination of minerals in the ASU spectral library fits the TES spectra, and a mixture of plagioclase feldspar, pyroxene, olivine, and sheet silicates or simply a Deccan flood basalt are plausible solutions that fully account for the spectral properties of the Martian data.

The match to sand-sized particles is consistent with the thermal inertia and albedo values derived for dark regions, with dark regions typically composed of coarse-grained (100–500 μm) particles [*Palluconi and Kieffer*, 1981; *Edgett and Christensen*, 1991]. The spectral contrast for this region is also consistent with the contrast of dark regions derived from Viking IRTM multispectral data [*Christensen*, 1982, 1998] and confirms the expectations of spectral contrasts in Martian surface materials that were used in the TES instrument design [*Christensen et al.*, 1992].

The TES data provide the first observation of feldspar on Mars. The abundance of plagioclase feldspar derived from the

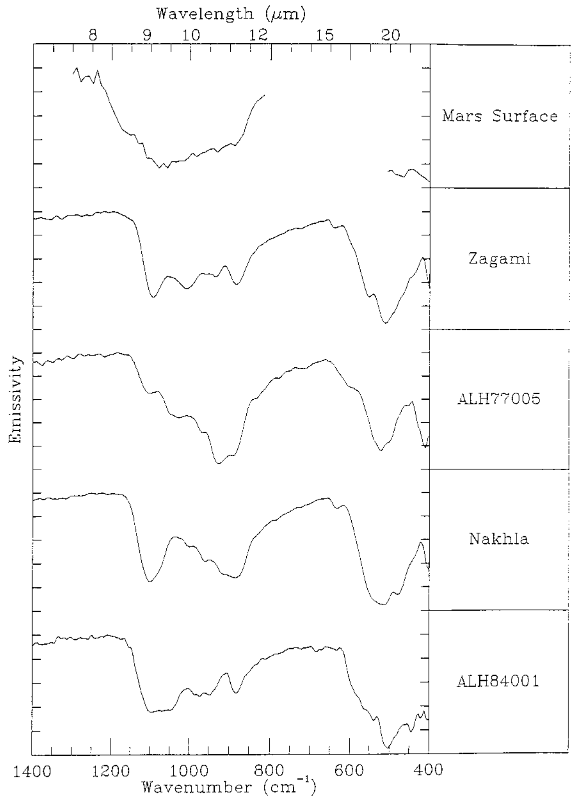

Figure 10. Comparison of Cimmeria Terra surface-only spectrum with four Martian meteorites [*Hamilton et al.*, 1997]. Zagami is a basalt, ALH7705 is a lherzolite, Nakhla is a clinopyroxenite, and ALH84001 is an orthopyroxenite. Spectra are offset and normalized for clarity.

TES data using the full mineral library varies from 45 to 53% depending on the atmospheric model, while the abundance of pyroxene varies from 19 to 26% (Table 3a). The plagioclase feldspar/pyroxene ratio varies from 2.8 to 1.8 between the atmospheric models that include the secondary components and from 1.9 to 1.2 for models with plagioclase feldspar and pyroxene alone. In all models, plagioclase feldspar is the dominant mineral present in the Cimmeria region.

The best fit to the Mars data includes only Ca-rich clinopyroxenes (augite and diopside), even though a full range of pyroxene compositions (except pigeonite) was included in the deconvolution model (Table 1). No orthopyroxene compositions are required to match the Cimmeria spectra. This result differs from the results of *Mustard and Sunshine* [1995] and *Mustard et al.* [1997], who found both low- and high-Ca pyroxenes in dark regions in Syrtis Major and Eos Chasma, but we emphasize that our detection limit for orthopyroxene is ~10%.

The composition of the Cimmeria surface materials, assuming that the observed mineral assemblage represents a single igneous lithology, is in the range of basalt to basaltic andesite. At present, the precise composition of the plagioclase feldspar mineral(s) cannot be accurately determined, so a more precise classification is unwarranted.

5.2. Other Components

Of equal interest are components that are noticeably lacking in the derived surface mineralogy of the Cimmeria region. Carbonates are not present in any detectable abundance in this region. The surface spectra discussed here cover only the spectral region from 400 to 1280 cm^{-1} because of the effects of variable atmospheric water vapor (section 2.1). Carbonates have a strong, narrow absorption feature within this spectral range at 880 cm^{-1} [*Farmer*, 1974] which is not observed. In addition, carbonates have a major absorption band centered at 310 cm^{-1}, and inspection of the full TES spectrum (Figure 3) shows no indication of this feature. On the basis of analysis of the TES data, together with sensitivity studies of the shape and depth of the carbonate spectral bands, we estimate an upper limit of ~5% for carbonates in this region in Cimmeria Terra.

Sulfates have a fundamental vibrational feature near 1150 cm^{-1} (e.g., 1145 cm^{-1} for gypsum). This feature is not observed in the Cimmeria surface spectra, and sulfates were not detected with any confidence in the deconvolution modeling. On the basis of analysis of spectral variations and the shape and depth of the sulfate band we estimate that sulfates are not present in this region above a detection limit of ~10%.

Minor abundances of quartz (<3%) were detected using the full ASU mineral library. However, these abundances are below the reliable detection limit, even for laboratory data. Quartz, in particular, is often retrieved at 2–3% abundance in laboratory rock samples when it is not present [*Feely*, 1997]. This error of commission is likely due to gross similarities between quartz and feldspar spectra which cause quartz to be included in the deconvolution model to help account for minor discrepancies between the composition of feldspars in the library and those present in the sample [*Ruff*, 1998]. Sensitivity studies of quartz suggest that it is not present above the 5% level.

The lack of detectable carbonate and sulfate components in the Cimmeria region may have only limited implications for the global occurrence of these minerals. Models of surface properties and processes suggest that dark regions on Mars are active, with ongoing sand movement leading to the removal of fine-grained dust [*Thomas*, 1984; *Christensen*, 1988]. This activity could result in the disruption and subsequent dispersal of near-surface, sulfur-rich crusts such as observed at the Viking landing sites [*Clark et al.*, 1982]. Similarly, carbonate materials may not be stable at the surface in dark regions with active mechanical abrasion. Thus, while significant amounts of carbonate and sulfate materials do not exist at the surface in the Cimmeria region, the question of their presence in more favorable surface environments remains open.

5.3. Comparison to SNC Meteorites

The SNC meteorites, commonly believed to be rocks ejected from the martian surface (see *McSween* [1994] for a review), encompass a range of mafic igneous lithologies including basalt/lherzolite (e.g., Shergotty, Zagami, and ALH77005), clinopyroxenite (e.g., Nakhla and Lafayette), dunite (Chassigny), and orthopyroxenite (ALH84001). Owing to the variability in their compositions, the thermal infrared emission spectra of SNC meteorites look considerably different and enable them to be distinguished from each other [*Hamilton et al.*, 1997]. Visual comparison of the derived Martian surface spectrum with the spectra of several of these meteorites (Figure 10) shows a poor qualitative match to any single SNC spectrum. The dissimilarity between the Martian surface spectrum and the SNC meteorite spectra suggests that the average composition of Terra Cimmeria is not typical of any single SNC lithology. Systematic searches for surface spectral signatures of Martian meteorites are ongoing.

5.4. Implications for Martian Surface Weathering

The TES data presented here show that unweathered minerals, pyroxene and plagioclase feldspar, are exposed at the surface in Terra Cimmeria. Previous visible/near-IR data have also indicated the occurrence of unweathered pyroxene minerals on the surface (see section 2). Overall, the TES data indicate that 85–100% of the surface materials in this region are unweathered igneous minerals. Relatively minor (0–15%) abundances of sheet silicates or other chemical weathering products could be present below the current detection limits in the TES data. The surfaces of dark regions on Mars clearly show a red color, indicating the presence of alteration products [*Bell*, 1996]. However, significant amounts of these materials are not consistent with the TES results or with visible/near-IR observations (see reviews by *Soderblom* [1992] and *Bell* [1996]).

Analysis of Viking multispectral data has shown that the darkest rocks are consistent with unoxidized basaltic andesite with minor (<30 nm) coatings of palagonite, although this match is not unique [*Adams et al*., 1986; *Guinness et al*., 1987, 1997]. *McSween et al*. [1999] favor a model in which the observed trends in visible/near-IR spectra of the rocks at the Pathfinder site are produced by varying amounts of relatively thin surface coatings. They suggest that two different coating episodes have occurred in which two different ferric minerals have covered rocks to varying degrees. These thin coatings are consistent with the TES findings of unweathered minerals exposed at the surface.

We therefore conclude that while weathering and coating of rocks has occurred, it has produced relatively minor amounts of weathering products, and unweathered materials are present at the surface in significant (>85%) abundance in at least one dark region (Cimmeria).

It is important to note that all of the three Mars landings have occurred in relatively bright regions. The albedos of the Viking 1, Viking 2, and Pathfinder sites are 0.27, 0.25, and 0.22, respectively [*Pleskot and Miner*, 1981], whereas the albedo of the Cimmeria site studied here is 0.15. Other regions on Mars are even darker, with albedos as low as 0.10 in Syrtis Major. Therefore it is likely that the surface rocks and sands in the dark regions such as Cimmeria Terra are less coated by bright dust than those seen at any site visited to date. It has been suggested that Mars dark regions are likely areas of active removal of bright dust by sand saltation or other means [*Thomas*, 1984; *Christensen*, 1988]. Landing sites in dark regions might provide an opportunity to directly sample exposed, dust-free rocks [*Edgett et al*., 1994].

In summary, the Viking, Pathfinder, hyperspectral visible/near-IR, and TES results show that the dark regions on Mars are dominated by unweathered materials. The large extent of dark regions, together with the occurrence of unweathered rocks in bright, dust-mantled regions, argues against extensive, globally pervasive weathering of materials now exposed at the surface of Mars.

6. Conclusions

The initial analysis of TES thermal infrared spectra for which two different atmosphere-removal models have been applied has led to the following conclusions:

1. The surface and atmospheric emission can be separated and an atmosphere-removed surface spectrum can be successfully produced. Differences in the derived mineral abundances for two different atmosphere-removal models are small (<10%), indicating that the exact atmospheric correction used has little effect on the derived surface composition.
2. The surface materials exposed in the dark region of Cimmeria Terra (24.8°S, 213.2°W), assuming they represent a single igneous lithology, are basaltic to basaltic andesite in composition.
3. The spectra from this region closely match both the spectral shape and contrast of a particulate sample of a terrestrial flood basalt. No unusual particle size or other environmental effects are observed, or are required, to account for the spectra observed for Mars.
4. Deconvolution models show that the Cimmeria region is composed of plagioclase feldspar, clinopyroxene, ±olivine, and ±sheet silicates. The TES data provide the first evidence for feldspar minerals exposed on Mars. Orthopyroxenes are not required to fit the Cimmeria spectrum. The derived feldspar and pyroxene abundances range from 45 to 65% and from 20 to 45%, respectively, for the different models discussed, with feldspar being the dominant mineral in all cases.
5. The Cimmeria Terra spectra are not well matched by any of the SNC meteorite spectra, which indicates that the average composition of this region is not typical of any single SNC lithology.
6. Carbonates, quartz, and sulfates are not observed in Cimmeria Terra at detection limits of ~5, 5, and 10%, respectively.
7. The TES data indicate that extensive chemical weathering has not occurred in the dark region of Cimmeria Terra.

Acknowledgments. We wish to thank the entire TES Engineering Team, lead by Steve Silverman and Martin Greenfield at Raytheon Santa Barbara Remote Sensing, and Greg Mehall at Arizona State University for their efforts in developing the TES instrument. Hugh Kieffer, Mike Malin, Ken Edgett, Steve Ruff, Melissa Lane, and Scott Nowicki participated in stimulating discussions on the topics discussed here. Jim Bell, III and Hap McSween provided excellent reviews that significantly improved the manuscript. We thank Greg Mehall, Kelly Bender, Noel Gorelick, Kamran Qazi, Saadat Anwar, Michael Weiss-Malik, Kim Homan, Kim Feely, and Tara Haden for their excellent work in planning, acquiring, and processing the TES data at ASU. We thank the Smithsonian Museum of Natural History for samples beginning with "NMNH." Finally, we wish to acknowledge our appreciation of the outstanding efforts of the MGS Spacecraft Teams at Lockheed Martin and NASA's Jet Propulsion Laboratory, which have led to the success of the MGS mission. This work was supported by the NASA Mars Global Surveyor Project Office and the NASA Planetary Geology and Geophysics Program.

References

Adams, J. B., Visible and near-infrared diffuse reflectance spectra of pyroxenes as applied to remote sensing of solid objects in the solar system, *J. Geophys. Res*., *79*, 4829–4836, 1974.

Adams, J. B., M. O. Smith, and P. E. Johnson, Spectral mixture modeling: A new analysis of rock and soil types at the Viking Lander 1 site, *J. Geophys. Res*., *91*, 8098–8112, 1986.

Bandfield, J. L., P. R. Christensen, and M. D. Smith, Spectral data set factor analysis and end-member recovery: Application to analysis of Martian atmospheric particulates, *J. Geophys. Res*., this issue.

Banin, A., B. C. Clark, and H. Wanke, Surface chemistry and mineralogy, in *Mars*, edited by H. H. Kieffer et al., Univ. of Ariz. Press, Tucson, 1992.

Bell, J. F., III, Iron, sulfate, carbonate, and hydrated minerals on Mars, in *Mineral Spectroscopy: A Tribute of Roger G. Burns*, edited by M. D.

Dyar, C. McCammon, and M. W. Schaefer, *Spec. Publ. Geochem. Soc.*, *5*, 359–380, 1996.

Christensen, P., Regional dust deposits on Mars: Physical properties, age, and history, *J. Geophys. Res.*, *91*, 3533–3545, 1985.

Christensen, P. R., Martian dust mantling and surface composition: Interpretation of thermophysical properties, *J. Geophys. Res.*, *87*, 9985–9998, 1982.

Christensen, P. R., Global albedo variations on Mars: Implications for active aeolian transport, deposition, and erosion, *J. Geophys. Res.*, *93*, 7611–7624, 1988.

Christensen, P. R., Variations in Martian surface composition and cloud occurrence determined from thermal infrared spectroscopy: Analysis of Viking and Mariner 9 data, *J. Geophys. Res.*, *103*, 1733–1746, 1998.

Christensen, P. R., Calibration report for the Thermal Emission Spectrometer (TES) for the Mars Global Surveyor Mission, Mars Global Surveyor Project, Jet Propul. Lab., Pasadena, Calif., 1999.

Christensen, P. R., and S. T. Harrison, Thermal infrared emission spectroscopy of natural surfaces: Application to desert varnish coatings on rocks, *J. Geophys. Res.*, *98*(B11), 19,819–19,834, 1993.

Christensen, P. R., et al., Thermal Emission Spectrometer experiment: The Mars Observer Mission, *J. Geophys. Res.*, *97*, 7719–7734, 1992.

Christensen, P. R., J. L. Bandfield, V. E. Hamilton, D. A. Howard, M. D. Lane, J. L. Piatek, S. W. Ruff, and W. L. Stefanov, A thermal emission spectral library of rock-forming minerals, *J. Geophys. Res.*, this issue (a).

Christensen, P. R., et al., Detection of crystalline hematite mineralization on Mars by the Thermal Emission Spectrometer: Evidence for near-surface water, *J. Geophys. Res.*, this issue (b).

Clark, B. C., A. K. Baird, R. J. Weldon, D. M. Tsusaki, L. Schnabel, and M. P. Candelaria, Chemical composition of Martian fines, *J. Geophys. Res.*, *87*(B12), 10,059–10,067, 1982.

Edgett, K. S., and P. R. Christensen, The particle size of Martian aeolian dunes, *J. Geophys. Res.*, *96*, 22,765–22,776, 1991.

Edgett, K. S., R. B. Singer, and P. E. Geissler, Opportunity to sample something different: The dark, unweathered, mafic sands of Cerberus and the Pathfinder 1997 Mars landing, in *Mars Pathfinder Landing Site Workshop*, p. 25, Lunar Planet. Inst., Houston, Tex., 1994.

Erard, S., J.-P. Bibring, and Y. Langevin, Determination of spectral units in the Syrtis Major-Isidis Planitia region from Phobos/ISM observations, *Lunar Planet. Sci.*, *XX*, 327, 1990.

Farmer, V. C., *The Infrared Spectra of Minerals*, 539 pp., Mineral. Soc., London, 1974.

Feely, K. C., Quantitative compositional analysis of igneous and metamorphic rocks using infrared emission spectroscopy, Masters thesis, Ariz. State Univ., Tempe, 1997.

Feely, K. C., and P. R. Christensen, Quantitative compositional analysis using thermal emission spectroscopy: Application to igneous and metamorphic rocks, *J. Geophys. Res.*, *104*, 24,195–24,210, 1999.

Gillespie, A. R., A. B. Kahle, and F. D. Palluconi, Mapping alluvial fans in Death Valley, CA, using multichannel thermal infrared images, *Geophys. Res. Lett.*, *11*(11), 1153–1156, 1984.

Gillespie, A. R., M. O. Smith, J. B. Adams, and S. C. Willis, Spectral mixture analysis of multispectral thermal infrared images, in *Proceedings of the Second TIMS Workshop*, edited by E. A. Abbott, *JPL Publ. 90-55*, pp. 57–74, Jet Propul. Lab., Pasadena, Calif., 1990.

Guinness, E. A., R. E. Arvidson, M. A. Dale-Bannister, R. B. Singer, and E. A. Bruchenthal, On the spectral reflectance properties of materials exposed at the Viking landing sites, *J. Geophys. Res.*, *92*, 575–587, 1987.

Guinness, E. A., R. E. Arvidson, I. H. D. Clark, and M. K. Shepard, Optical scattering properties of terrestrial varnished basalts compared with rocks and soils at the Viking landing sites, *J. Geophys. Res.*, *102*, 28,687–28,703, 1997.

Hamilton, V. E., and P. R. Christensen, Determining the modal mineralogy of mafic and ultramafic igneous rocks using thermal emission spectroscopy, *J. Geophys. Res.*, this issue.

Hamilton, V. E., P. R. Christensen, and H. Y. McSween Jr., Determination of Martian meteorite lithologies and mineralogies using vibrational spectroscopy, *J. Geophys. Res.*, *102*, 25,593–25,603, 1997.

Hook, S. J., K. E. Karlstrom, C. F. Miller, and K. J. W. McCaffrey, Mapping the Piute Mountains, California, with thermal infrared multispectral scanner (TIMS) images, *J. Geophys. Res.*, *99*, 15,605–15,622, 1994.

Hovis, W. A., Jr., and W. R. Callahan, Infrared reflectance spectra of igneous rocks, tuffs, and red sandstone from 0.5 to 22 μ, *J. Opt. Soc. Am.*, *56*, 639–643, 1966.

Hunt, G. R., and J. W. Salisbury, Mid-infrared spectral behavior of igneous rocks, *Environ. Res. Pap.*, *496-AFCRL-TR-74-0625*, 142, 1974.

Hunt, G. R., and J. W. Salisbury, Mid-infrared spectral behavior of sedimentary rocks, *Environ. Res. Pap.*, *520-AFCRL-TR-75-0356*, 49, 1975.

Lyon, R. J. P., and E. A. Burns, Analysis of rocks by reflected infrared radiation, *Econ. Geol.*, *58*, 274–284, 1963.

McCord, T. B., R. Clark, and R. L. Huguenin, Mars: Near-infrared reflectance and spectra of surface regions and compositional implications, *J. Geophys. Res.*, *87*, 3021–3032, 1982.

McSween, H. Y., Jr., What have we learned about Mars from SNC meteorites?, *Meteoritics*, *29*, 757–779, 1994.

McSween, H. Y., Jr., et al., Chemical, multispectral, and textural constraints on the composition and origin of rocks at the Mars Pathfinder landing site, *J. Geophys. Res.*, *104*, 8679–8716, 1999.

Moersch, J. E., T. Hayward, P. Nicholson, S. W. Squyres, J. V. Cleve, and P. R. Christensen, Identification of a 10 μm silicate absorption feature in the Acidalia region of Mars, *Icarus*, *126*, 183–196, 1997.

Mustard, J. F., and J. M. Sunshine, Seeing through the dust: Martian crustal heterogeneity and links to the SNC meteorites, *Science*, *267*, 1623–1626, 1995.

Mustard, J. F., J.-P. Bibring, S. Erard, E. M. Fischer, J. W. Head, S. Hurtrez, Y. Langevin, C. M. Pieters, and C. J. Sotin, Interpretation of spectral units of Isidis-Syrtis Major from ISM-Phobos 2 observations, *Lunar Planet. Sci.*, *XXI*, 835–836, 1990.

Mustard, J. F., S. Erard, J.-P. Bibring, J. W. Head, S. Hurtrez, Y. Langevin, C. M. Pieters, and C. J. Sotin, The surface of Syrtis Major: Composition of the volcanic substrate and mixing with altered dust and soil, *J. Geophys. Res.*, *98*, 3387–3400, 1993.

Mustard, J. F., S. Murchie, S. Erard, and J. M. Sunshine, In situ compositions of Martian volcanics: Implications for the mantle, *J. Geophys. Res.*, *102*, 25,605–25,615, 1997.

Palluconi, F. D., and H. H. Kieffer, Thermal inertia mapping of Mars from 60°S to 60°N, *Icarus*, *45*, 415–426, 1981.

Pleskot, L. K., and E. D. Miner, Time variability of Martian bolometric albedo, *Icarus*, *45*, 179–201, 1981.

Ramsey, M. S., Quantitative analysis of geologic surfaces: A deconvolution algorithm for midinfrared remote sensing data, Ph.D. dissertation, Ariz. State Univ., Tempe, 1996.

Ramsey, M. S., and P. R. Christensen, Mineral abundance determination: Quantitative deconvolution of thermal emission spectra, *J. Geophys. Res.*, *103*, 577–596, 1998.

Ramsey, M. S., P. R. Christensen, N. Lancaster, and D. A. Howard, Identification of sand sources and transport pathways at Kelso Dunes, California using thermal infrared remote sensing, *Geol. Soc. Am. Bull.*, *111*, 636–662, 1999.

Reider, R., T. Economou, H. Wanke, A. Turkevich, J. Crisp, J. Bruckner, G. Drebus, and H. Y. McSween Jr., The chemical composition of Martian soil and rocks returned by the mobile alpha proton X-ray spectrometer: Preliminary results from the X-ray mode, *Science*, *278*, 1771–1774, 1997.

Ruff, S. W., Quantitative thermal infrared emission spectroscopy applied to granitoid petrology, Ph.D. dissertation, Ariz. State Univ., 1998.

Salisbury, J. W., L. S. Walter, and D. D'Aria, Mid-infrared (2.5 to 13.5 μm) spectra of igneous rocks, *U.S. Geol. Surv. Open File Rep.*, *88-686*, 1988.

Singer, R. B., The dark materials on Mars, II, New mineralogic interpretations from reflectance spectroscopy and petrologic implications, *Lunar Planet. Sci.*, *XI*, 1048–1050, 1980.

Singer, R. B., Spectral evidence for the mineralogy of high-albedo soils and dust on Mars, *J. Geophys. Res.*, *87*, 10,159–10,168, 1982.

Singer, R. B., and H. Y. McSween Jr., The igneous crust of Mars: Compositional evidence from remote sensing and the SNC meteorites, in *Resources of Near-Earth Space*, edited by J. Lewis, M. S. Matthews, and M. L. Guerrieri, pp. 709–736, Univ. of Ariz. Press, Tucson, 1993.

Singer, R. B., and T. L. Roush, Analysis of Martian crustal petrology, *Bull. Am. Astron. Soc.*, *17*, 737, 1985.

Singer, R. B., T. B. McCord, R. N. Clark, J. B. Adams, and R. L. Huguenin, Mars surface composition from reflectance spectroscopy: A summary, *J. Geophys. Res.*, *84*, 8415–8426, 1979.

Smith, J. V., and R. L. Hervig, Shergotty meteorite: Mineralogy, petrology, and minor elements, *Meteoritics*, *14*, 121–142, 1979.

Smith, M. D., J. L. Bandfield, and P. R. Christensen, Separation of atmospheric and surface spectral features in Mars Global Surveyor Thermal Emission Spectrometer (TES) spectra, *J. Geophys. Res.*, this issue.

Soderblom, L. A., The composition and mineralogy of the Martian surface from spectroscopic observations: 0.3 μm to 50 μm, in *Mars*, edited by H. H. Kieffer et al., pp. 557–593, Univ. of Ariz. Press, Tucson, 1992.

Stöffler, D., R. Ostertag, C. Jammes, G. Pfannschmidt, P. R. S. Gupta, S. B. Simon, J. J. Papike, and R. H. Beauchamp, Shock metamorphism and petrography of the Shergotty achondrite, *Geochim. Cosmochim. Acta*, *50*, 889–904, 1986.

Stolper, E., and H. Y. McSween Jr., Petrology and origin of the shergottite meteorites, *Geochim. Cosmochim. Acta*, *43*, 1475–1498, 1979.

Thomas, P., Martian intracrater splotches: Occurrence, morphology, and colors, *Icarus*, *57*, 205–227, 1984.

Thomson, J. L., and J. W. Salisbury, The mid-infrared reflectance of mineral mixtures (7–14 μm), *Remote Sens. Environ.*, *45*, 1–13, 1993.

J. L. Bandfield, P. R. Christensen, and V. E. Hamilton, Department of Geology, Arizona State University, Campus Box 871404, Tempe, AZ. (phil.christensen@asu.edu)

R. N. Clark, U.S. Geological Survey, Denver, CO.

M. D. Smith, NASA Goddard Space Flight Center, Greenbelt, MD.

(Received June 21, 1999; revised September 13, 1999;
accepted October 12, 1999.)